# Journal Pre-proof

How to tame a free non-laminar Savart sheet into individual jets?

Sofiene Ouled Taleb Salah, Ghada Chouk, Alexis Duchesne,
Nicolas De Cock, Khaoula Abrougui, Frédéric Lebeau,
Stéphane Dorbolo

Please cite this article as: S.O.T. Salah, G. Chouk, A. Duchesne et al., How to tame a free non-laminar Savart sheet into individual jets?. *International Journal of Multiphase Flow* (2022), doi: https://doi.org/10.1016/j.ijmultiphaseflow.2022.104032.

This is a PDF file of an article that has undergone enhancements after acceptance, such as the addition of a cover page and metadata, and formatting for readability, but it is not yet the definitive version of record. This version will undergo additional copyediting, typesetting and review before it is published in its final form, but we are providing this version to give early visibility of the article. Please note that, during the production process, errors may be discovered which could affect the content, and all legal disclaimers that apply to the journal pertain.

# How to tame a free non-laminar Savart sheet into individual jets?

Sofiene Ouled Taleb Salah,[1, 2, a)] Ghada Chouk*,[3] Alexis Duchesne*,[4, b)] Nicolas De Cock,[2] Khaoula Abrougui,[3] Frédéric Lebeau,[2] and Stéphane Dorbolo[1]

[1)] *University of Liege, CESAM - GRASP, Institute of Physics, Building B5a, Sart Tilman, 4000 Liege, Belgium.*

[2)] *University of Liege, TERRA Teaching and Research Center, Gembloux Agro - Bio Tech, Passage des déportés 2, 5030 Gembloux, Belgium.*

[3)] *Department of Horticultural Systems Engineering, Higher Institute of Agronomy, 4042 Sousse, Tunisia.*

[4)] *Univ. Lille, CNRS, Centrale Lille, Univ. Polytechnique Hauts-de-France, UMR 8520 - IEMN, F-59000 Lille, France.*

In this article, we study the division of a non-laminar Savart sheet into individual jets by mean of local disturbances. We paint a precise portrait of a free non-laminar Savart sheet formed by the vertical impact of a jet on a horizontal disk, its evolution in the air and its break up.

We then generate local disturbances, outside of the disk circumference, triggered by $N$ radial triangular prisms placed directly in the non-laminar sheet. We show that, under given flow conditions and geometrical parameters for the triangular prisms, the sheet splits into individual jets. Depending on the incoming flow rate $Q$ and on the geometry of the prism, the number of jets $n$ can be either stable (and equal to $N$ jets) or variable due to elastic coalescing of neighboring jets. Phase diagrams $(Q,n)$ are obtained from experimental measurements for different geometrical parameters of triangular prisms. A semi-empirical model, which explains the generation of individual jets, is established. Finally, we characterize the droplets emitted from the non-laminar Savart sheet and from the jets in terms of diameters.

Keywords: Savart sheet, free surface flow, jets, droplets

* These authors contributed equally to this work

## I.  INTRODUCTION

The perturbation of a liquid film has been the subject of numerous experimental, numerical and theoretical studies. This is due to both a fundamental interest and numerous industrial applications such as surface coating[14]. As an example, the stability of steady free falling liquid curtains destabilized by air blowing has recently attracted a lot of attention[11].

The perturbation of a liquid film may also be relevant in an agricultural context particularly if we aim to design hydraulic nozzles. The operating mode of these nozzles is simple as it consists in forcing the passage of a pressurized spray mixture through a calibrated pore. As a result, a non-laminar liquid sheet is produced and it disintegrates randomly into ligaments leading to droplets of various diameters and velocities[6]. However, to increase the efficiency of agricultural spraying (and therefore reduce its use and its economic and environmental costs) it is necessary to precisely control the sizes of the emitted droplets[13].

The design of new nozzles able to generate a narrow droplet size distribution is therefore a challenging track for the precision agriculture[20,29]. In this context, it may be of interest to perturb a liquid sheet in order to split it into individual jets, which disintegrate into droplets of controlled sizes and trajectories.

---

[a)] soufien.talbi@yahoo.fr

[b)] alexis.duchesne@univ-lille.fr

In the present article, we will focus on the disturbance of horizontal liquid sheets in a gaseous atmosphere namely Savart sheets. These liquid sheets may be obtained by impinging two opposed jets[31], by impinging a liquid jet on a cone[26], at a smaller scale by impinging droplets on a plate[30] or simply by impinging a round liquid jet with a diameter $d$ onto a solid disk with a diameter $D^{1,2,4,9,16,17,21-23,27,28}$. In the latter case, the impacted jet formed a liquid film, which spreads radially along the disk surface, the liquid inertia being balanced by the viscosity and the drag force emanating essentially from the friction on the disk surface. If the disk is small enough (typically for a ratio $X = \frac{D}{d} \sim 1$) and the jet speed sufficient, inertia forces exceed capillary forces at the edges of the impinged disk and then the liquid film leaves the disk and forms a curved and self-suspended liquid sheet with a maximum radial expansion $R$ from the jet axis. The shape of the sheet results from the balance between inertial, capillary and gravitational effects and friction with the surrounding atmosphere. For non-laminar flows, the sheet is not stable and local disturbances at the impact trigger the puncturing[13,25] further in the free sheet (i.e. outside of the disk)[19]. Eventually, the holes amplify and lead to a chaotic disintegration of the sheet into ligaments. In both cases (laminar and non-laminar) the Savart sheet eventually breaks up into droplets of miscellaneous sizes[4,9,28].

As previously mentioned, controlling the size of the emitted droplets is crucial for numerous applications such as designing agronomic engines. Therefore, we focus on how upstream perturbations in the film may impact the droplet size distribution.

Partially answering to this question, numerous experimental and numerical studies deal with the perturbation of a Savart sheet formed by a jet impinging a surface[7,10,12,15,23,24]. As a result, it comes out that the easiest way to perturb a Savart sheet is to texture the disk surface. For instance, we can cite the pioneer work of Taylor[23] where knife cuts were engraved radially and regularly on the disk surface along its circumference and resulted in a Savart sheet with cardioid shapes at the surface[23]. We can also refer to the work of Dressaire et al.[7], where the jet impact on a regular micro-texturing disk leads to polygonal shaped water bells with preferred droplet emission sites located at the vertices of the created polygonal structures[7].

If the previous examples addressed the issue of the effects of perturbation on laminar Savart liquid sheet only, some efforts were also put into the case of non-laminar flows. A recent experimental study focused on the perturbation of a non-laminar Savart sheet by using engraved radial grooves along the impacted disk circumference[19]. It was possible, under specific flow conditions, to split the non-laminar sheet into individual jets that break up into quasi-monodisperse droplets.

In the present paper, we aim to divide a free Savart sheet formed by the vertical impact of a liquid jet on a horizontal disk under non-laminar flows conditions. The novelty of our approach lies in the fact that we place the perturbations after the detachment of the sheet from the impinged disk, i.e. in the air. We indeed propose to fragment the liquid sheet into jets by creating local disturbances (triangular prisms) downstream the disk border and before the appearance of holes inherent to non-laminar Savart sheet. Under given flow conditions and geometrical parameters of these textures (detailed later), the radial flow in the sheet locally turns into individual jets. By this mean, we are able to decompose the non-laminar sheet into controlled size droplets. In addition and even if it is not the main object of our study, we are the first, to our knowledge, to handle a non-laminar Savart sheet and partially characterize its dynamics and breakups.

Regarding the potential applications in the agricultural field, this study may pave the way to a new kind of agricultural nozzle design since we are not limited anymore by the size of the impinged disk to split the sheet into a large number of liquid jets, in that sense this study presents major advances compared to ref.[19].

We structured the article as follows: In the first part, we describe the used material and methods. In the second part, we characterize the non-laminar Savart sheet. Then, we detail our technique to split a non-laminar sheet into jets by using triangular prisms. We introduce a geometrical model that explains the generation of individual jets through these structures. Finally, we characterize the diameter of the emitted droplets.

## II. MATERIAL AND METHODS

### A. Setup

We used most of the features of an experimental setup previously developed in[19]. The experimental setup is presented in Figure 1.

The nozzle geometry consisted in a glass injector characterized by an internal diameter of $d = 3$ mm and a length of 155 mm set perpendicularly to a horizontal motionless disk. The injector generated a cylindrical liquid jet which impacted the disk center with a mean velocity $U_0 = \frac{4Q}{\pi d^2}$; with $Q$ the injected flow rate. This jet is characterized by the Reynolds number $Re = \frac{U_0 d}{\nu}$; with $\nu$ the kinematic viscosity. The disk, made with a veroblue print polymer, was 3D printed (Objet30 Prime TM). The disk diameter $D$ was fixed to 6 mm and, therefore, $X = 2$. The value of $D$ was a compromise between the flow velocity and the development of the Savart sheet: the disk diameter must be small enough to minimize the radial flow deceleration due to friction effects at the disk surface but large enough to ensure the formation of the Savart sheet. We fixed the disk on a support in the middle of a 200 mm side cubic tank and its horizontality was checked by a spirit level. A three-axis precision displacement tool XYZ tuned the gap between the injector tip and the disk surface. The gap was set to 550 $\mu$m, which is the critical distance reachable with the gear pump.
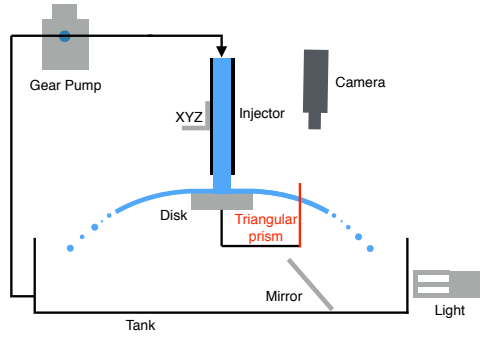


FIG. 1: Sketch of the experimental setup: The nozzle geometry consisted in a glass pipe injector generating a round jet $d = 3$ mm. The injected water impacted the center of a veroblue print polymer disk. We placed the disk in the middle of a 200 mm side cubic tank. The gap between the injector tip and the disk surface was fixed to 550 $\mu$m. A high-speed camera was mounted vertically to sheet and droplet trajectories to acquire shadow images of liquid sheet and emitted droplets. A mirror was tilted by 45° to the camera optic axis in order to reflect the light towards the disk. A gear pump connecting the tank to the injector injected the liquid. We used triangular prisms mounted outside the disk surface to break up the free Savart sheet.

A gear pump (Ismatec BVP-Z), combined with a pump head (Z-142 - ref MI 0018), injected the liquid in a reduced-pulsations and stable way. The flow was measured by weighing the liquid poured into a graduated tank during 30 s and three repetitions were performed for each flow measurement. Flow rates $Q$ were varied from 1.5 $10^{-5}$m$^3$. s$^{-1}$ to 4.1 $10^{-5}$m$^3$. s$^{-1}$. The $Re$ numbers inside the injector have been estimated to range between 9000 and 16000. This regime corresponds to a non-laminar jet and therefore a non-laminar impact on the disk[18].

The used liquid was tap water at 20 °C (density $\rho = 1000$ kg.m$^{-3}$, kinematic viscosity $\nu = 10^{-6}$ m$^2$.s$^{-1}$ and surface tension $\sigma = 73.5 \pm 0.3$ mN.m$^{-1}$). By using an optical contact angle meter (CAM 200 KSV), we estimated the static contact angle on veroblue to be approximately 25°.

We used specific structures to perturb the free Savart sheet. Their characteristics are detailed below, in section 4.

## B. Savart sheet and droplet characterization

In this article the liquid Savart sheet was conical. The sheet was regular until a distance $R'$ from the impact, punctured between the distance $R'$ to $R$ and finally, fragmented into droplets further (for detail, see next section). To characterize this object we used two optical configurations in order to :

(i) Measure the ejection angle of the sheet $\phi$ relative to jet axis. The measurement process was eye-guided using a high-speed camera Y4 (IDT motion) aligned with a LED light. The camera optic axis was set perpendicularly to the disk surface axis.

(ii) Measure the radii $R'$ and $R$ from the top. The axis of the high-speed camera Y4 was set parallel to the disk axis. A mirror was tilted by $45°$ to camera optic axis and it reflected the light emitted from the LED light source towards the disk (see Figure 1). The images were acquired at a frequency of 2000 Hz and treated with a Matlab code.

Finally, we used the same high-speed camera Y4 coupled to the LED light to record shadows of the tap water droplets. The image acquisition frequency was then 5000 Hz. Images were analyzed with a Particle Tracking Velocimetry Sizing (PTVS) algorithm developed in Matlab and provided droplet size and velocity components perpendicular to optic axis[5]. The statistics of the droplet measurements were established for a number of drops superior to 8000. The position of droplet measurements varied as a function of the disk type. In the case without prisms, droplets were measured as soon as they detached from the sheet (60 mm from the disk edge). In the case of prisms, droplets were measured as soon as they were detached from the jet.

## III. NON-LAMINAR SAVART SHEET

In the following lines, we describe experimentally the characteristics of the Savart sheet obtained using the presented device. We would like to stress out that the theory allowing the prediction of $R'$ and $R$ is to be discovered and is beyond the scope of this study. In our approach, the shape of the Savart sheet is viewed as an important piece of information in order to place the obstacles in the free puncture zone of the Savart sheet for the considered range of flow rates. In this section, we first focus on the evolution of the curved shape of the Savart sheet and, then, on its radial expansion.

Figure 2 presents the evolution of the angle $\phi$, i.e. the angle of the curved sheet relative to the jet axis, as a function of $Q$. The acquired images from a side view of the nozzle are embedded in Figure 2 in order to provide a better comprehension of the sheet evolution. No variability was observed when measuring $\phi$. For low $Q$ values, the sheet is subject to the gravity and the obtained shape is a closed/semi-opened water bell as illustrated on the first image on the left in Figure 2 ($\phi = 54°$). When $Q$ increases, the water bell progressively opens and the gravity effect becomes negligible compared to inertia. It presents a slightly inclined shape highlighted by a value of $\phi$ inferior to $90°$ for high $Q$ values. Hence, in this configuration (i.e. with a flat impactor), we cannot reach a horizontal ejection of the sheet accordingly to the literature[3].

Figure 3b presents a typical picture of the sheet. This picture suggests the definition of two radii showed in the sketch Figure 3a: $R'$ below which the sheet is continuous and plain and $R$ below which the sheet is only continuous but randomly punctured with some holes. $R$ corresponds to the radial position of the sheet rim and is delimited by nodes from which droplets are emitted (Figure 3b) as observed in the laminar case[9].

The region between $R'$ and $R$ is characterized by holes of various sizes, which amplify and lead to the disintegration of the liquid sheet into ligaments and droplets at a distance $R$ from the center. We interpret this phenomenon as the consequence of the non-laminar flow
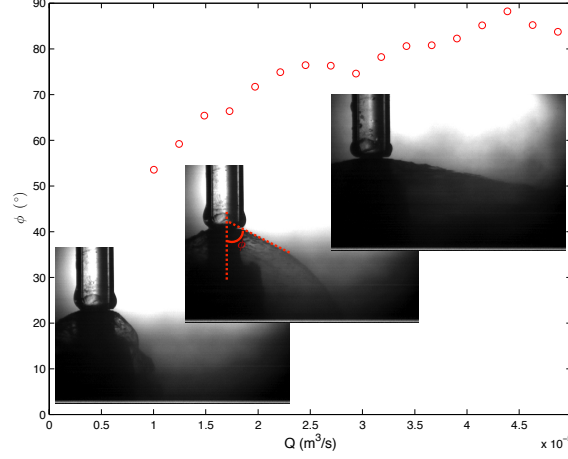
FIG. 2: Evolution of the angle $\phi \pm 1°$, quantifying the opening angle of the curved Savart sheet relative to the jet axis, as a function of $Q$. The side-view images of the nozzle show the evolution of the sheet from a curved bell to a conical sheet.

at the jet impact, from where perturbations increase and puncture the thin liquid sheet for larger radii.

Figure 3c shows the evolution of $R$ and $R'$ as a function of $Q$. These radii values were computed from 100 images separated by 0.5 ms. This fairly short timescale was chosen in order to better track the evolution of sheet holes. Error bars indicate the standard deviation calculated using 100 measurement repetitions of $R$ and $R'$ for the same $Q$. The radii $R$ and $R'$ take into account $\phi$ and $D$ (for instance: $R = \frac{D}{2} + \frac{(R_{measured} - \frac{D}{2})}{\cos \phi}$ with $R_{measured}$ the radius extracted from the images).

The radius $R$, corresponding to sheet expansion, increases almost linearly with $Q$ for $Q < 3 \ 10^{-5} \ \mathrm{m^3.s^{-1}}$. Then, for high $Q$ values, the sheet presents a (slightly decreasing) plateau with $R$ values around 40 - 50 mm corroborated by large error bars. The curve of $R'$ shows similar trends: $R'$ increases with $Q$ when $Q < 3 \ 10^{-5} \ \mathrm{m^3.s^{-1}}$ and the curve slightly decreases for high $Q$ values with values for $R'$ around 30 mm.

To facilitate comparisons with the laminar Savart liquid sheet situation, we added in Figure 3c experimental measurementsof the sheet radius $R$ from Clanet and Villermaux[4]. The $D$ and $d$ were respectively 10.8 mm and 2.7 mm ($X = 4$). We underline the fact that, despite these similar conditions (especially the same flow rate range), Clanet et al. generated a laminar Savart sheet thanks to their injector especially designed for this purpose. The two curves of $R$ (for laminar and non-laminar regimes) present similar trends even if the non-laminar regime presents smaller $R$ values.

The similarities between the results obtained by Clanet and Villermaux[4] and our results lead us to think that the mechanisms at play are similar in both situations: for low $Q$, $R$ and $R'$ increase as $Q$ until the aerodynamic drag and momentum of the ejected drops become non-negligible. After a critical $Q$, we observe that $R$ and $R'$ are constant or slowly decreasing with $Q$.

## IV. IMPACT ON A DISK WITH PRISMS

As presented in the Introduction, our aim is to divide the free Savart sheet into individual jets by creating local defects out of the disk circumference. To reach this goal we investigate
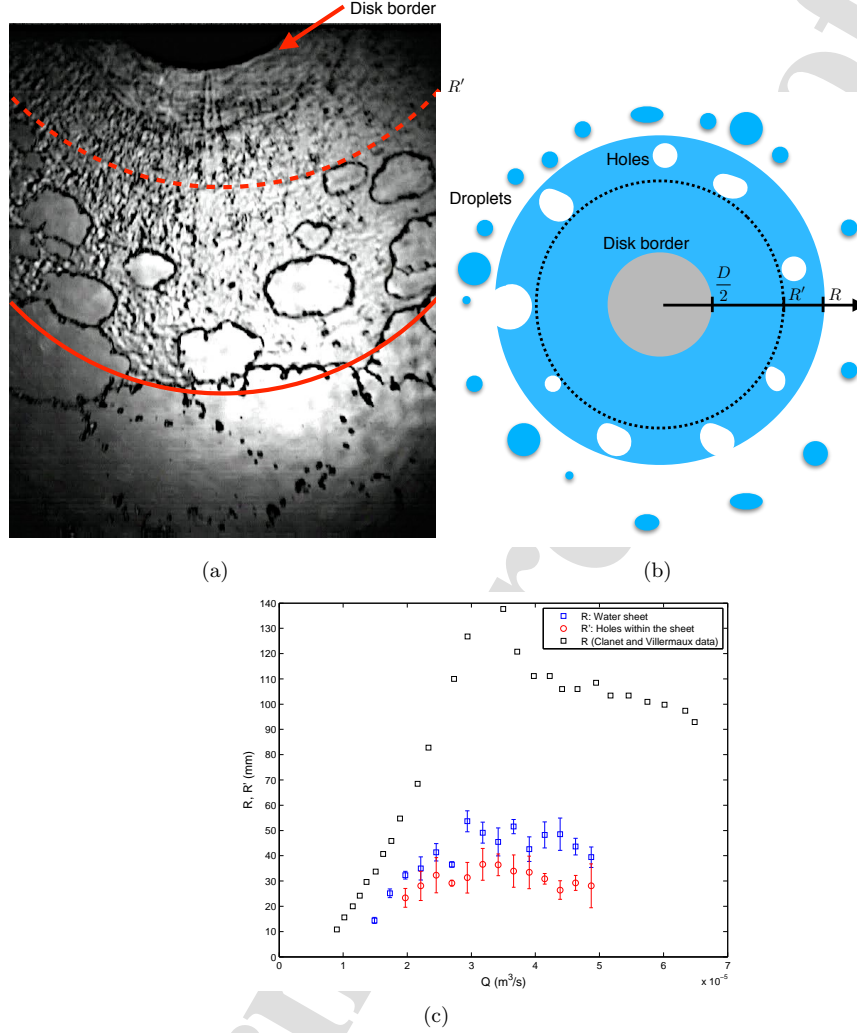
(a)  (b)



(c)

FIG. 3: Top view of a non-laminar Savart liquid sheet. A picture (a) and a sketch (b) present the radial sheet expansion $R$ and the appearance of holes at a radial distance $R'$. $X = 2$ and the jet was characterized by $U_0 = 4.22$ m.s$^{-1}$ and $Re = 12\,414$. (c) Evolution of the radii $R$ (blue) and $R'$ (red) of the Savart sheet as a function of $Q$. Experimental measurements of Clanet and Villermaux[4] for the radius $R$ in laminar regime are added. The values of $D$ and $d$ in Ref[4] were respectively 10.8 mm and 2.7 mm corresponding to a $X = 4$.

the influence of triangular prisms placed downstream the disk border at a radial distance $R_p$ from the injector axis (Figure 4a).

Following the preliminary results developed in the previous section we chose $R_p = 15$ mm. Indeed, the distance $R_p$ is to be set between: $\frac{D}{2} < R_p < R'$ in order to destabilize the liquid sheet in the continuous and plain region.

The triangular prisms made of veroblue polymer were printed on a 3D printer Objet30 Prime TM. Their upper surfaces were isosceles triangles characterized by a base $a_p$ and a
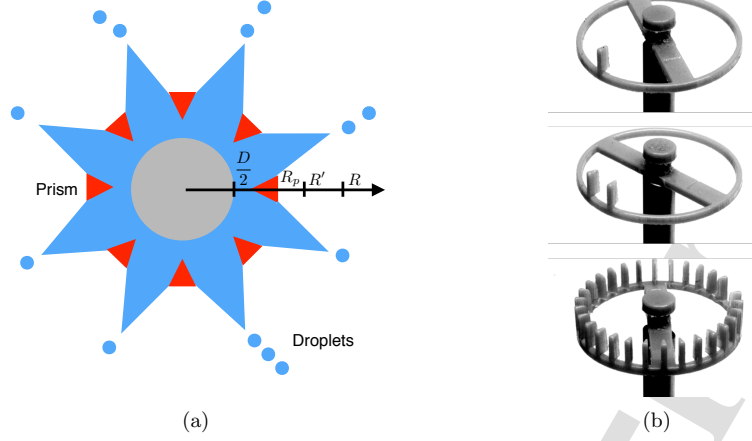
FIG. 4: (a) Top view of the non-laminar Savart sheet perturbed by triangular prisms. (b) Pictures from the side of the structures used to control the non-laminar sheet. Single triangular prism (top), two triangular prisms (middle) and $N$ triangular prisms (bottom).

perpendicular bisector to the base $l_p$ which was fixed to 2.5 mm all along the article (see sketch Figure 5).

The height of the triangular prisms $A$ was set to 20 mm. It was large enough to guarantee that the liquid sheet properly impacted the prism, even by taking into account the opening angle $\phi(Q)$ of the Savart sheet.

In the following subsections, we will investigate, in turn, the case of a single triangular prism, the cases of two prisms and finally of $N$ triangular prisms symmetrically arranged along the circumference (see Figure 4b).

### A.  Case of a single triangular prism

A triangular prism characterized by $a_p = 0.99$ mm is placed directly in the Savart sheet at $R_p = 15$ mm. This local perturbation provokes the sheet opening. This opening may be characterized by an angle $\beta$ (Figure 6a) and no wake is observed downstream the prism i.e. the space downstream the prism is empty of liquid (Figure 6 (a), (b) and (c)). It is worth noticing that this opening is different of the steady wake observed in the case a free falling curtain[11].

Figure 7 presents the behavior of $\beta$ as a function of $Q$ in the case of a single prism. The value of $\beta$ was measured based on one image for a given flow rate $Q$ since the opening shape was stable. For low flows $Q$, the sheet portion close to the prism curves rapidly as the surface tension tends to reduce interfaces (Figure 6a). For higher $Q$, $\beta$ value decreases and get much closer to the prism angle as the inertia increases and balances surface tension effects (Figure 6b and 6c).

### B.  Case of two neighboring triangular prisms

We now consider the situation where the radial liquid sheet is intercepted by two neighboring triangular prisms. The distance between two successive prisms is $b$ and defines an arc of circle of angle $2\alpha$ (Figure 8).

When two successive triangular prisms ($a_p = 0.99$ mm) spaced by a gap $b$ are inserted in
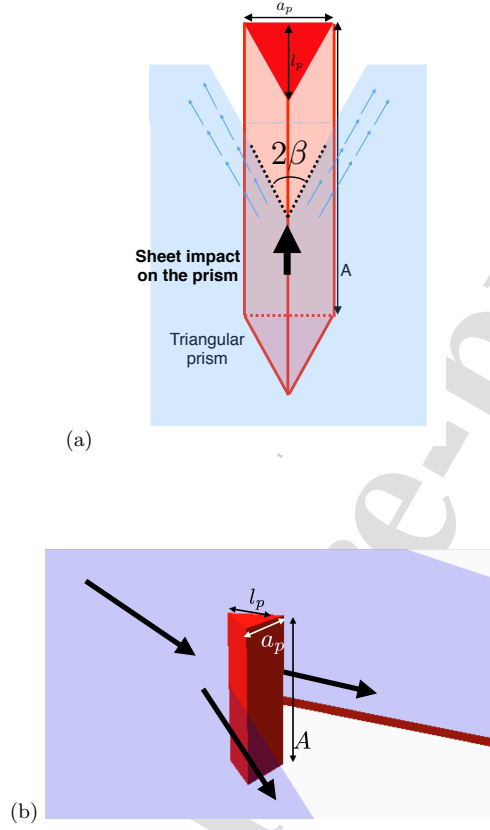
FIG. 5: Sketches of a triangular prism from the point of view of an observer placed at the liquid jet impact position (a) and placed outside of the liquid sheet slightly above it (b). The top surface of the triangular prisms is an isosceles triangle with a base $a_p$ and a perpendicular bisector $l_p$. The total length of the prism is defined as $A$.

the Savart sheet, two neighboring openings are created leading to the formation of a sheet slice entrapped in the gap $b$ (Figure 9). The ejection angle of this sheet slice is $\phi(Q)$, i.e. the ejection angle of the Savart sheet without perturbations.

For low $b$ values, a liquid beam similar to a capillary jet is generated. It eventually breaks up into droplets under the action of the surface tension (Figure 9a). As $b$ increases, a more developed liquid sheet is observed. The sheet is therefore characterized by a delta shaped tongue (designed by $vss$: $v$ $shaped$ $sheet$) with a maximal expansion $C$ (Figure 9b). At the convergence of the $vss$, we observe a ligament characterized by a breakup length $L_b$ (Figure 9b). For high $b$ values, the trapped liquid penetrates easily through the gap, and hence leads to a well-developed sheet dominated by inertia (close to a typical Savart sheet)(Figure 9c). As a classical Savart sheet, the latter's rim destabilizes into ligaments and nodes due to the surface tension.

In this configuration, it is also possible to define the opening angle $\beta$ in a way similar to its definition in a single prism situation. We observe that the liquid sheet is symmetric and that the values of $\beta$ are the same for the both openings (see Figure 9). We report our results in Figure 7 for seven gaps $b$ as a function of $Q$. All curves adopt a trend similar to the one observed in the case of a single prism i.e. $\beta$ is high at low Q and decreases
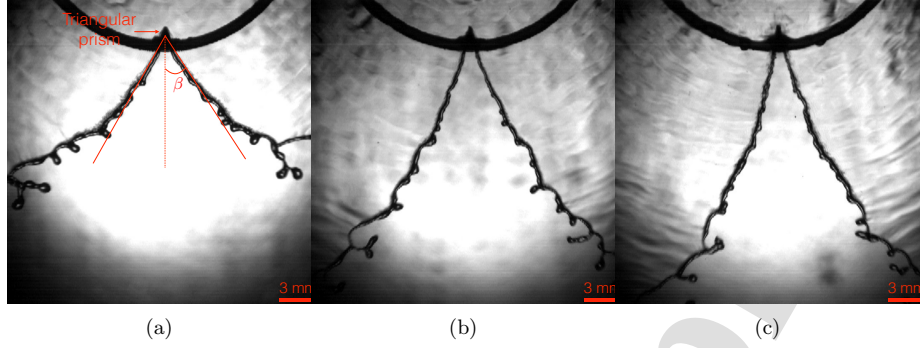
FIG. 6: Top views of the perturbation of a Savart sheet using a triangular prism structure characterized by $a_p = 0.99$ mm and $l_p = 2.5$ mm and placed directly in the sheet at 15 mm from the jet axis for different flow rates $Q$: 2 $10^{-5}$ m$^3$.s$^{-1}$ (a), 3.7 $10^{-5}$ m$^3$.s$^{-1}$ (b) and 4.8 $10^{-5}$ m$^3$.s$^{-1}$ (c).
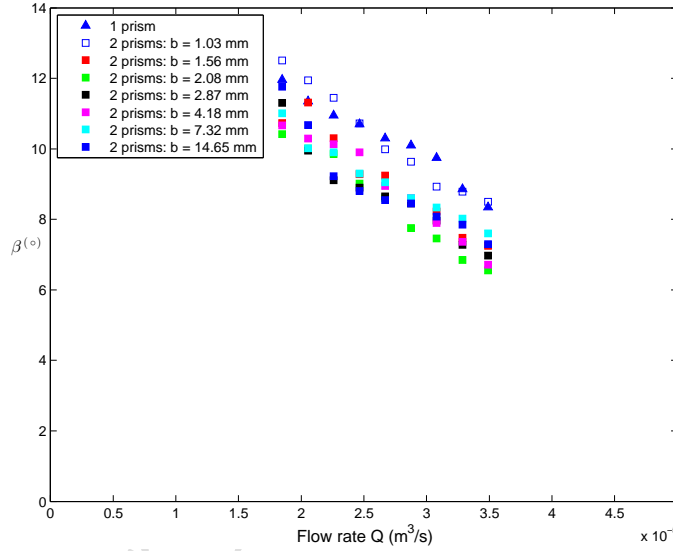


FIG. 7: Evolution of the sheet opening $\beta$ as a function of the flow rate $Q$.

when $Q$ increases, i.e. when inertia dominates the surface tension. We also remark that the introduction of a second prism affects only slightly the sheet opening since the $\beta$ values for all the cases are very close for the same $Q$.

In a first attempt to model the formation of the $vss$ through the gap between two neighboring triangular prisms, we developed a simple geometrical model. The $vss$ is approximated by a delta shape. The model aims to establish interactions between $C$ that is an intrinsic parameter of the $vss$ and the geometrical parameters of the triangular prisms as presented in Figure 8. Such a model assumes that all the physics lie in $\beta$, which is fixed by the geometry and the competition between inertia and surface tension.

Based on a trigonometric development, we define $C$ is as follows

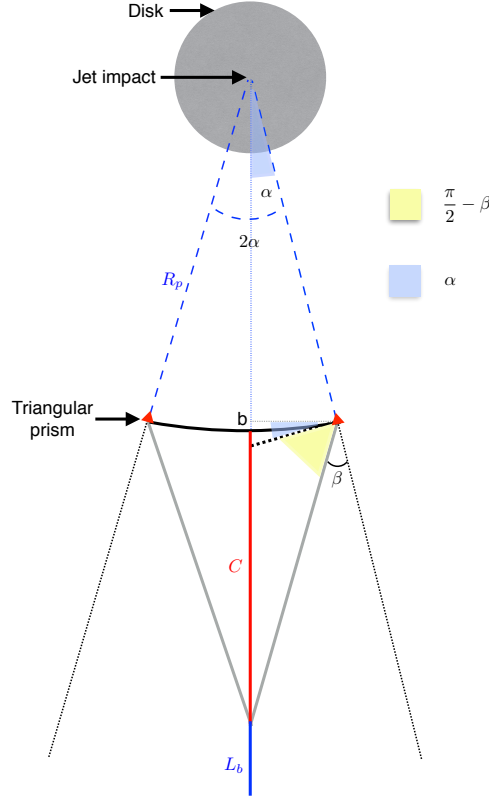$$C = R_p \left( \sin \alpha \tan\left(\frac{\pi}{2} - \beta + \alpha\right) - (1 - \cos \alpha) \right). \tag{1}$$

FIG. 8: In top view: the distance between two successive prisms is $b$ and defines an arc of circle under the angle $2\alpha$. One defines geometrical parameters of the sheet used in the semi-empirical model.

The limits of the model depend on the angles $\alpha$ and $\beta$:
- When $\alpha$ tends to zero, the $C$ value is zero. It reflects the case where the sheet hits the triangular prisms because $b = 0$.
- When $\alpha < \beta$, the model results in a defined $C$ value since the $vss$ is developed.
- When $\alpha \geq \beta$, $C$ tends towards infinity but one is limited by the expansion sheet $R$. Hence, $C$ tends towards $R$.

It is clear that this geometrical model overestimates $C$ since the $vss$ is curved (under the effect of surface tension) just getting far away from the lateral sides of the prisms (the value of $\beta$ is quickly modified). In addition, the model is semi-empirical since the experimental measurements of $\beta$ (that depends on $Q$) were used to compute $C$.

Figure 10 presents the evolution of $C$ as a function of $Q$ for different gaps $b$. The filled and unfilled markers represent respectively experimental and semi-empirical measurements (model) of $C$. For a given $Q$, each experimental measurement of $C$ is based on Matlab analysis of 50 images acquired at 2000 Hz. The values of $C$ are computed as follows: $C = \frac{C_{measured}}{\cos\phi}$.

For small $b$ values corresponding to small $\alpha$ values ($\leq 1.55$mm), the sheet expansion $C$ tends to zero as expected. The variability of $C$ is small, even for high $Q$ values, and the
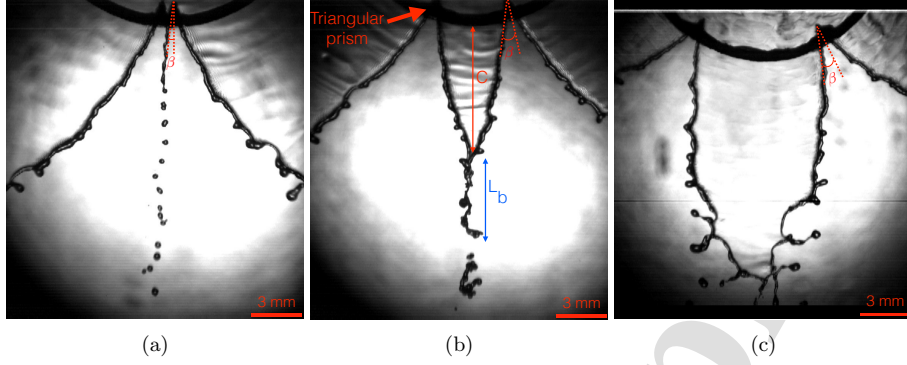
(a)        (b)        (c)

FIG. 9: Perturbation of a Savart sheet by two successive triangular prisms spaced by a gap $b$: (a) For $b = 250$ $\mu$m, a jet is directly generated through the gap. (b) For $b = 4.18$ mm, a $vss$ is formed and its radial expansion is designed by $C$. The sheet converges to form a jet ligament of length $L_b$, which eventually disintegrates into droplets. (c) For $b = 7.32$ mm, the obtained sheet is well developed and the $vss$ is less pronounced. Its rim breaks up into droplets. The trials were performed at the same $Q = 2.93 \ 10^{-5}$ m$^3$.s$^{-1}$.
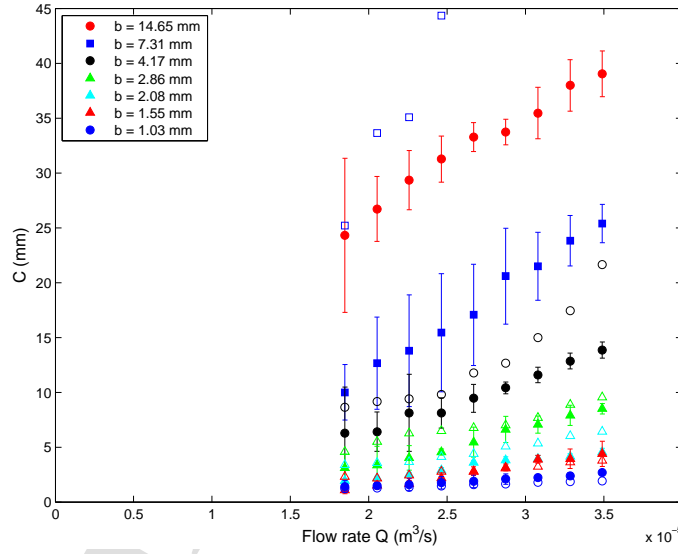


FIG. 10: Evolution of the maximum sheet expansion $C$ as a function of the flow rate $Q$ for different gap $b$ values. The filled and unfilled markers correspond respectively to the experimental and semi-empirical measurement of the maximum sheet expansion $C$.

empirical measurements and the semi-empirical model are in good agreement. In the case of $b \leq 4.17$ mm, the sheet expansion increases slightly with the increase of $Q$. The fit between semi-empirical model and experimental measurements is less observed. By increasing $b$, the sheet is well developed downstream the neighboring structures. The fit is no longer valid since the semi-empirical model overestimates the values of $C$ that tend to infinity in this case. For this reason, the curve corresponding to the case where $b = 14.65$ mm is not plotted. Also, for high $Q$, the holes appear near the sheet rim and disintegrate the sheet

what may reduce $C$. It is worth noticing that the expansion $C$ increases as $b$ increases for a given $Q$.

We can conclude that, when the agreement between the semi empirical model and the experimental data points is good (i.e. for small $b$), all the physics lie in the angle $\beta$. On the contrary, when the data points are in bad agreement with the theory, that means that surface tension acts on the liquid sheet itself and reduces $C$. Therefore the angle $\beta$ is insufficient to describe the entire phenomenon in this regime.
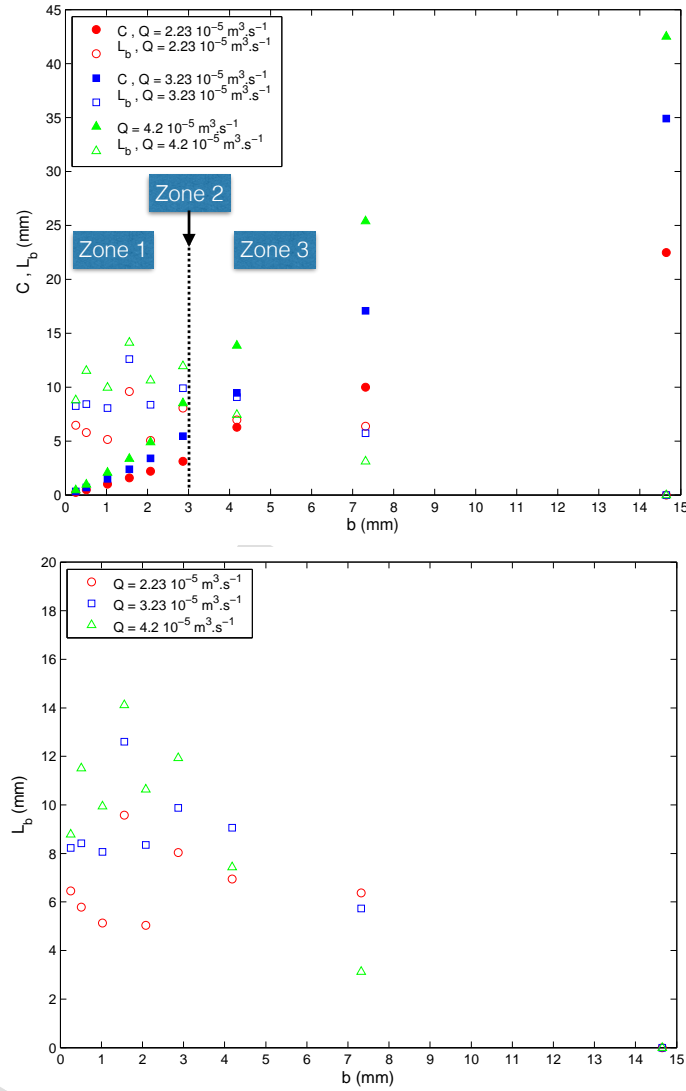


FIG. 11: Evolution of C and $L_b$ measured experimentally as a function of the geometrical distance $b$ between two successive prisms, for three different flow rates.

To understand the transition between the $vss$ and the jet that emerges from this latter, we compare in Figure 11 the distances $C$ and $L_b$ as a function of $b$ for different $Q$ values.

The Figure 12 presents, in log log scale, the evolution of $C$ as a function of the Weber number We = $\frac{\rho b U_0^2}{\sigma}$ (with $\rho$ the liquid density and $\sigma$ the liquid surface tension).
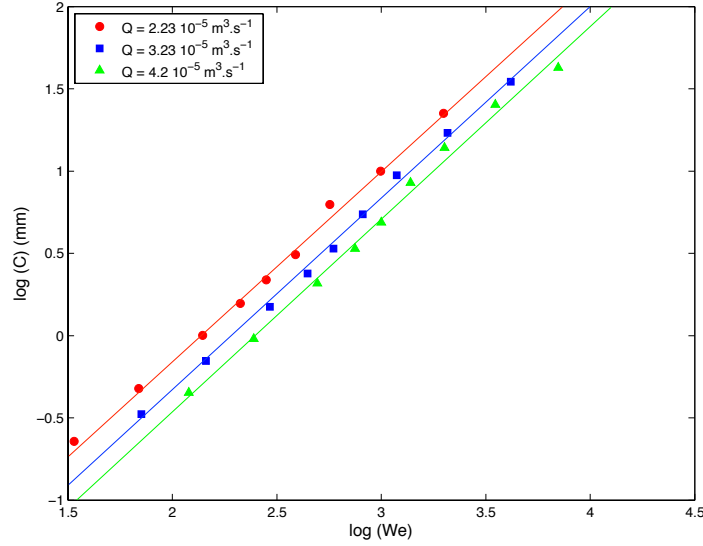


FIG. 12: Evolution of $C$ measured experimentally as a function of the Weber number $We$ between two successive prisms (log log scale) for three different flow rates. Lines are power law fits. Red disks: $C \propto We^{1.14}$, blue squares: $C \propto We^{1.17}$ and green triangles: $C \propto We^{1.17}$.

The values of $L_b$ were based on Matlab analysis of 50 images acquired at 2000 Hz for a given $Q$. They are computed as follows: $L_b = \frac{L_{b\ measured}}{\cos\phi}$.

The parameters $C$ and $L_b$ present two opposite trends with the increase of $b$. Three main zones may be defined. The first one corresponds to small $b$ values for which $C$ is inferior to $L_b$. When $b$ tends to zero, there is no space for anything else than a jet ligament of length $L_b$. Therefore $C$ tends to zero. In addition, by increasing $Q$ for these small angles, the length $L_b$ increases. Then, when $b$ increases, the value of $C$ linearly increases (i.e. the $vss$ appears) (following the trend given in Eq. 1). Afterwards, both curves $C$ and $L_b$ intersect and we define the second zone that corresponds to gaps $b$ between 2.87 mm and 4.18 mm (their values are close to the capillary length, ~ 3 mm for the tap water). Finally, the $C$ values exceeds those of the $L_b$ i.e. the system promotes the generation of the $vss$ that emits a short jet ligament. Here, the $C$ increases with the increase of $Q$ and no trend is found for $L_b$ in this region.

From these observations, it is clear that the competition between the inertia and capillary forces plays a crucial role in the transition between these regimes. As a rule of thumb, when $b$ is very small compared to the capillary length (first zone), the capillarity dominates the flow and a jet ligament is generated through the gap. When $b$ is very large compared to the capillary length (third zone), the inertia exceeds the capillary forces and a well-developed $vss$ is generated.

From Figure 12, we also conclude that $C$ follows a power law in $We$ close to one ($C \propto We^{1.15}$). It shows, once again, that this complex phenomenon is solely due to the complex interplay between inertial and capillary effects. This power law is complementary with the semi-empirical model developed before, the semi empirical model furnishing good indications for the prefactor of the presented power law (at least for the small flow rates).
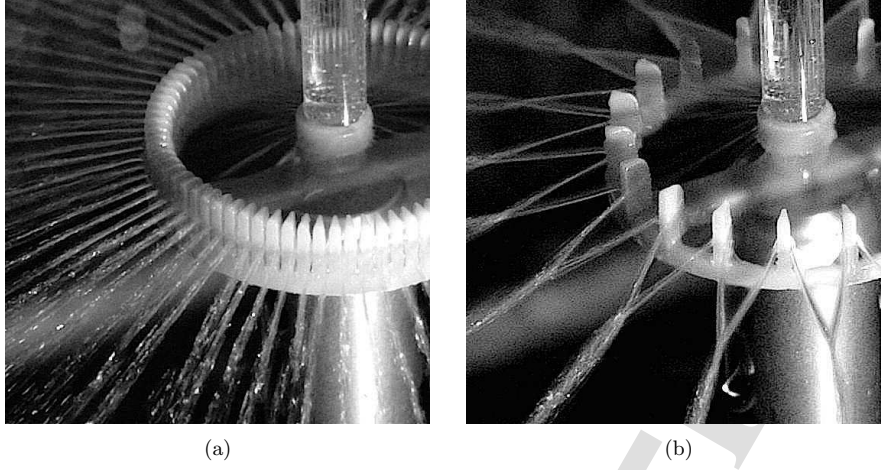
14



(a)                                                    (b)

FIG. 13: $N$ triangular prisms are used to control the non-laminar Savart sheet for $Q = 2.26 \ 10^{-5}$ m$^3$.s$^{-1}$. (a) Gap $b = 0.51$ mm: The entrapped liquid between prisms generates liquid jets (bead). (b) Gap $b = 4.17$ mm: The entrapped liquid between prisms generates $vss$.

## C.  Case of $N$ triangular prisms

In this last subsection, we consider the case of $N$ triangular prisms, regularly and symmetrically disposed, to divide the free Savart sheet. They are characterized by $a_p = 1.06$ mm and $l_p = 2.5$ mm. The local perturbations generated by these triangular prisms causes the formation of $n$ liquid jets/$vss$ (Figure 13). Depending on the flow rate and geometrical parameters, this number of jets $n$ may be either stable or fluctuating.

Varying $b$ (and therefore varying $N$) and $Q$, two regimes are observed and may be classified by the number $n$, as shown in Figure 14. The first regime is characterized by $n$ equal to $N$ and corresponds to low values of flow rates $Q$. In this regime the $n$ jets are stable. We may observe two cases depending on $b$ values: for low $b$, we observe liquid jets and, for high $b$ values, $vss$ converging in liquid jets. The second regime, established for high values of $Q$, is characterized by $n$ smaller than $N$ and greater or equal to $\frac{N}{2}$. In this regime, the jets/$vss$ may locally interact and merge and, as a result, $n$ is not anymore constant and fluctuates. We also observe two scenarii within this fluctuating jet regime: for small $b$ values, small jet columns emerge through the gaps and they may coalesce elastically, whereas for large $b$ values, $vss$ are generated through the gaps and coalesce elastically. At high $Q$ ($>> 3.8 \ 10^{-5}$ m$^3$.s$^{-1}$) whatever the value of $b$, the merging between sheet portions is no longer elastic what may lead to a Savart sheet downstream the prisms (not shown here).

The elastic coalescence may be caused by the corrugations presented at the surface of the generated jets. These corrugations constitute the elastic connection areas between two very close jets. We may also explain this elastic coalescence by the fact that the triangular prisms are wet and hence they constitute a connection source with the neighboring jet[8].

These results are quantified in Figure 15 for $a_p = 0.99$ mm. The smallest gap $b$ that can be printed is 0.25 mm leading to $N = 76$ prisms.

The transition between the regime $n = N$ and the regime $n < N$ is denoted by the continuous black line. We also recover the transition between the $vss$ and the jets that is solely fixed by the value of $b$ and occurs for $b= 0.5$mm.

We also investigate the influence of $a_p$ on the two regimes previously described. Due to the potential applications of our study we chose a low $b$ value ($b = 0.25$ mm) in order to maximize the number of prisms $N$ (and therefore the number of jets). The length $l_p$ was
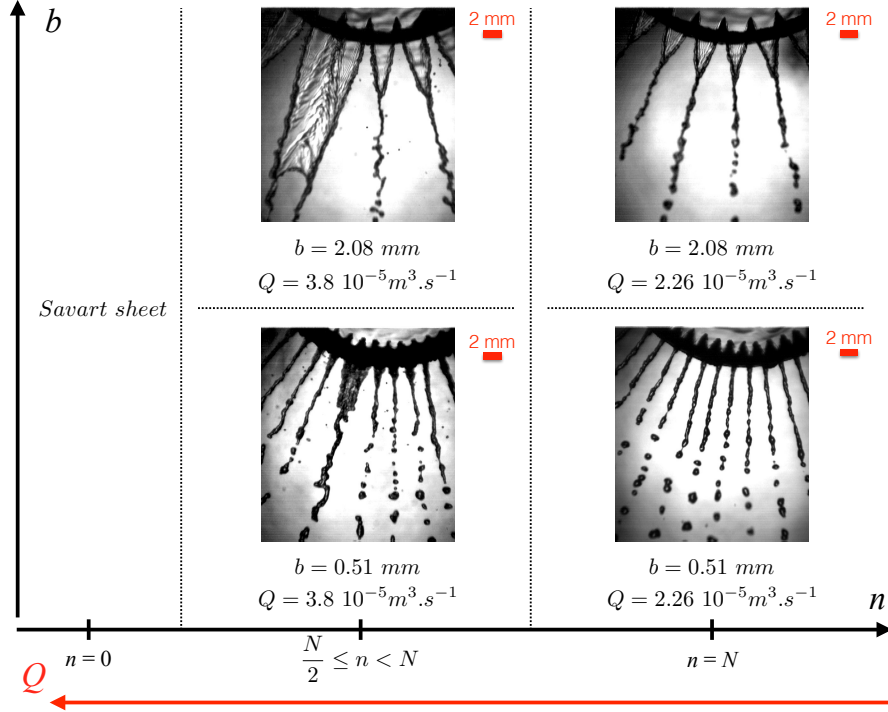
FIG. 14: Number of jets $n$ generated through the gaps between prisms depending on $b$ and $Q$. The number of jet $n$ can be stable and equal to $N$ or not and $n \leq N$.

kept to 2.5 mm. Varying $a_p$, we also change the prism number $N$ as described in the Table I.

TABLE I: Characteristics of prism designs based a variable $a_p$. The $b$ is fixed to 1 mm and the prisms are placed at 15 mm from the jet impact axis

| $a_p$ (mm) | Prism numbers $N$ |
|---|---|
| 0.28 | 180 |
| 0.34 | 160 |
| 0.59 | 112 |
| 0.75 | 94 |
| 0.85 | 86 |
| 0.99 | 76 |
| 1.06 | 72 |

As a first result, we observe only liquid jets. It confirms that the transition between liquid jets and $vss$ is solely fixed by the value of $b$. Both regimes ($n = N$ and $n < N$) are also visible and the transition is fixed by the flow rate $Q$. These results are coherent with our previous observations in Figures 13 and 15 : for low flow rates, we find the regime $n = N$ and for high flow rates $n < N$.

The phase diagram $Q$-$a_p$ presented in Figure 16 allows us to quantify these observations. The transition between the regime $n = N$ and the regime $n < N$ is denoted by the continuous black line. This diagram also highlights the role of $a_p$: the smaller $a_p$ is, the smaller is the critical flow rate which sets the transition to elastic coalescence of jets. For the lowest
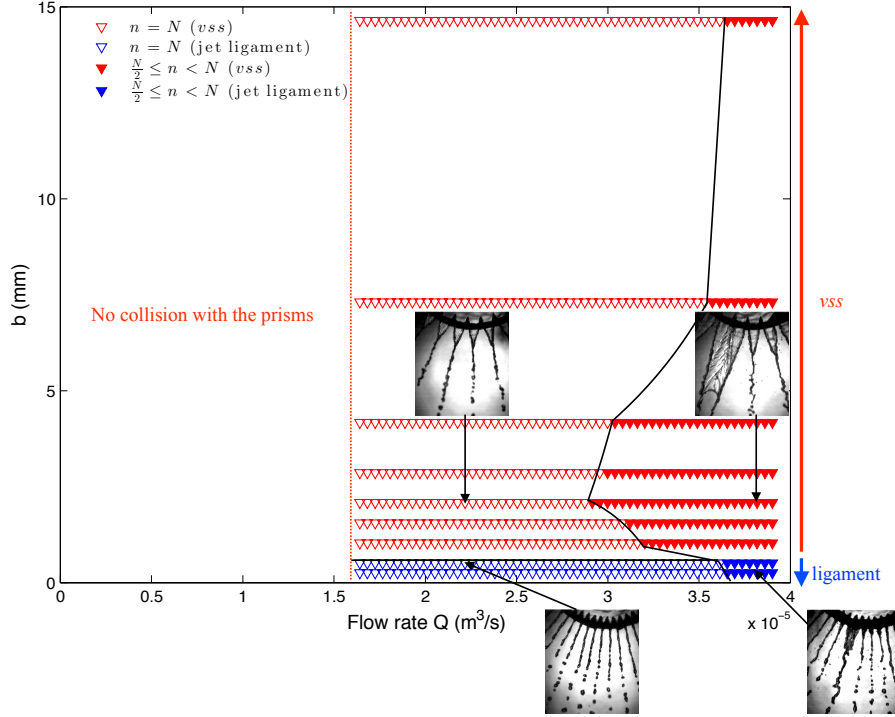
FIG. 15: Phase diagram of different jet zones as a function of $b$ (mm) and $Q$ (m$^3$.s$^{-1}$). The base $a_p$ is fixed to 0.99 mm.

values of $a_p$, we are even unable to observe the $n = N$ regime. Keeping in mind the two mechanisms that lead to elastic coalescence, this result is simple to interpret. For small $a_p$, the distance between two jets is reduced and therefore the liquid can easily wet the prisms and the corrugations can easily make two adjacent jets interacting.

To sum up, the liquid entrapped in the gap changes its radial expansion and adopts a tangential behavior that converges to a jet. This latter can be a $vss$ or a ligament jet and the transition between the two kinds of jets is directly linked to the competition between inertia and capillarity. The jet number can either be stable ($n = N$) for low $Q$ or not ($\frac{N}{2} \leq n < N$) for high $Q$. The reduction of $a_p$ allows to increase the jet numbers $n$ but leads to an expansion of the $n < N$ regime.

It is of interest to compare these results to the ones previously obtained for engraved radial grooves[19]. We can observe that the ranges of $Q$ necessary to a stable jet number $n = N$ or to the elastic coalescence between neighboring jets are roughly the same (though the $n = N$ regime is slightly larger for triangular prisms). The main difference leads in the fact that the present setup allows much higher number of jets $N$.

To extend this study, it is also worth noticing that prisms may be inserted further in the free Savart sheet ($> 15$ mm). The only limitation is to keep $R_p < R'$ (for which the holes appear in the sheet). The distance $R_p = 30$ mm is considered as the critical position for which the placement of prisms is too close to the hole zone (Figure 3c).
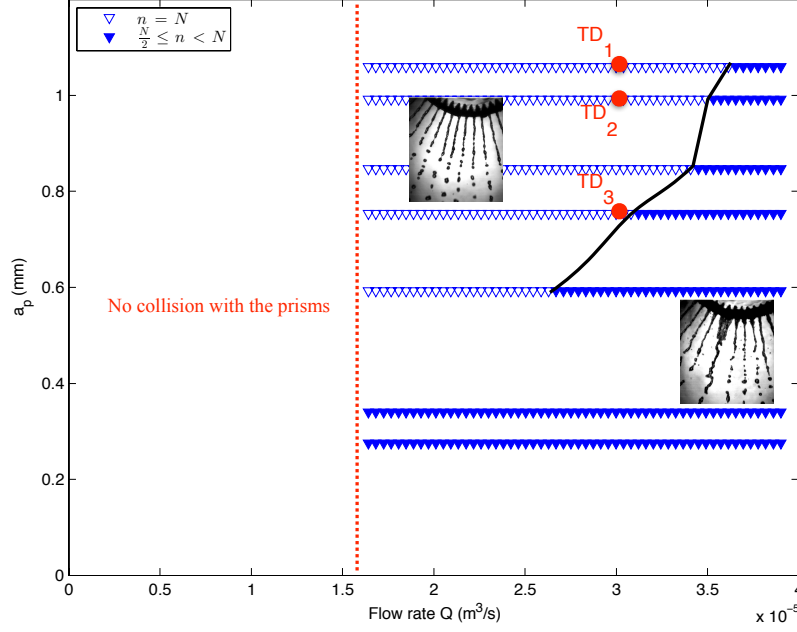
FIG. 16: Phase diagram of different jet zones as a function of $a_p$ (mm) and $Q$ (m$^3$.s$^{-1}$). The base $b$ is fixed to 0.25 mm. The points $TD_1$, $TD_2$ and $TD_3$ correspond to measurements of droplet sizes that will be detailed in section 5.

## V. DROPLET DIAMETER DISTRIBUTION

We now address the question of the size distribution of the droplets emitted in our experimental setup. We define relevant tools as the mean droplet diameter:

$$D_m = \frac{1}{N_d} \sum_{i=1}^{N_d} D_{d,i}, \tag{2}$$

with $N_d$ the number of droplets and $D_d$ the droplet diameter. We also use the Standard deviation:

$$STD = \sqrt{\frac{\sum_{i=1}^{N_d}(D_{d,i} - D_m)^2}{N_d}}, \tag{3}$$

and, finally, we define the coefficient of variation

$$CV = \frac{STD}{D_m}. \tag{4}$$

In the following, we first explore the diameter distribution of droplets emitted from two triangular prisms, then from $N$ triangular prisms with $R_p = 15$ mm and finally the diameter distribution of droplets emitted from $N$ triangular prisms with variable $R_p$.

### A. Case of two successive triangular prisms

We study here the diameter distribution of droplets issued from a jet/$vss$ formed after the perturbation of a Savart sheet by two successive triangular prisms. The parameters of
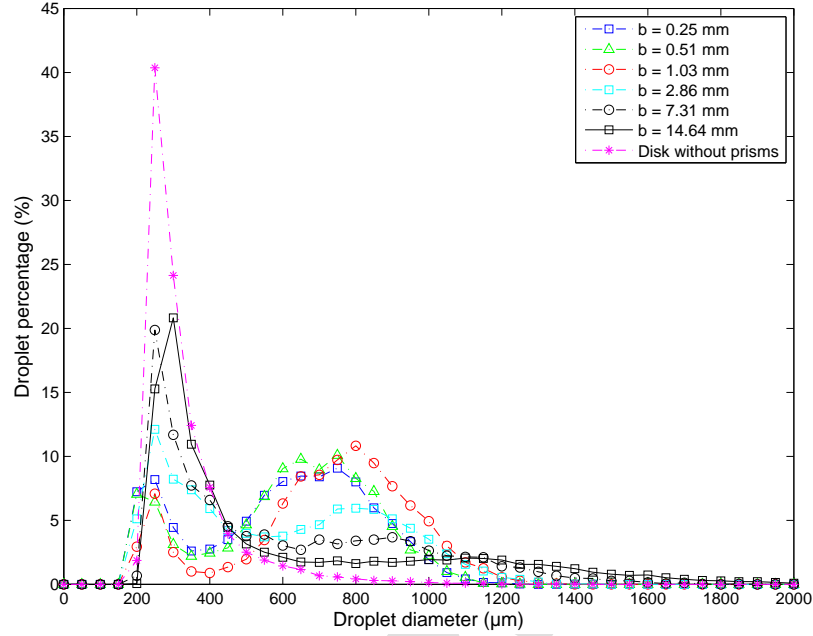
FIG. 17: Representation of droplet percentages as a function of their diameters in the case of two neighboring triangular prisms spaced by a gap $b$. The base of the prism $a_p$ is 1.06 mm. The prisms are placed at $R_p = 15$ mm from the jet impact. The curve *disk without prisms* corresponds to droplets emitted from the Savart sheet. All the measurements were performed for $Q = 2.8 \ 10^{-5} \ \mathrm{m}^3.\mathrm{s}^{-1}$.

this study are: $a_p = 1.06$ mm and $Q = 2.8 \ 10^{-5} \ \mathrm{m}^3.\mathrm{s}^{-1}$ and $b$ was varied between 0.25 mm and 14.64 mm.

Figure 17 presents a histogram where the percentage of droplets is plotted as a function of their diameters. All the configurations are compared to the reference measurement, i.e. a disk without prisms where droplets are ejected from the Savart sheet. Characteristics of droplets corresponding to different measurement points are shown in Table II. The mean droplet diameter $D_m$ is informative but does not represent the droplet size distribution since the distribution is bimodal.

TABLE II: Characteristics of droplets emitted in the case of two triangular prisms spaced by a gap $b$. The prisms are placed at $R_p = 15$ mm from the jet impact. The configuration *disk without prisms* corresponds to droplets emitted from the Savart sheet. All the measurements were performed for $Q = 2.8 \ 10^{-5} \ \mathrm{m}^3.\mathrm{s}^{-1}$.

| | $D_m$ ($\mu$m) | $STD$ ($\mu$m) | $CV$ (%) |
|---|---|---|---|
| *Disk without prisms* (X= 2) | 331 | 123 | 37 |
| *Disk without grooves* (X= 10) [19] | 503 | 318 | 63 |
| $b = 0.25$ mm | 602 | 233 | 38 |
| $b = 0.51$ mm | 621 | 225 | 36 |
| $b = 1.03$ mm | 717 | 239 | 33 |
| $b = 2.86$ mm | 588 | 280 | 47 |
| $b = 7.31$ mm | 583 | 331 | 56 |
| $b = 14.64$ mm | 600 | 413 | 68 |

In the case of the disk without prisms, the droplet size distribution has a probability peak corresponding to a droplet diameter of 250 $\mu$m and a percentage of 40 %. The mean droplet diameter $D_m$ is 331 $\mu$m. The droplet size distribution is tightened, as illustrated by reduced $STD$ and $CV$ values (respectively 123 $\mu$m and 37 %). Droplets with diameters exceeding 700 $\mu$m have low percentages of probabilities (inferior to 3 %).

These results may be compared to the ones previously obtained in[19] where $D = 30$ mm (in the present study $D = 6$ mm). In the present study the mean droplet diameter is much smaller (502 $\mu$m in[19]) and the distribution is much narrower ($STD = 318$ $\mu$m and $CV = 63$ % in[19]). We explain these differences by a reduced disk diameter in the present study. Indeed, a smaller diameter induces less friction on the liquid film and therefore a thinner film departing from the disk. Such a thinner film is expected to fragment into smaller droplets.

Figure 17 shows that the presence of two triangular prisms affects the droplet diameter distribution. The distribution is larger than the one for the Savart sheet and a second probability peak appears. For all $b$ values the first peak is close to the probability peak of the Savart liquid sheet (~300 $\mu$m) but its amplitude is much smaller and decreases when $b$ decreases. The position of the secondary peak depends on the values of $b$, it ranges from ~700 $\mu$m to ~1100 $\mu$m, and increases with the value of $b$. Its amplitude is also affected by $b$, it decreases from 10 % for the lowest $b$ values to less than 2 % for highest $b$.

We explain this bimodal distribution as follows : for high $b$ values the situation is very close to a Savart liquid sheet and the triangular prisms affect only marginally the flow and therefore the droplet diameter distribution. The second peak is, therefore, very small and the profile very close to the free Savart sheet. When $b$ decreases, the influence of triangular prisms is more pronounced: the obstacles force the liquid in a $vss$ converging in a liquid jet or in a liquid jet configuration. These liquid jets have a diameter fixed by $b$ and their disintegration by the Plateau-Rayleigh instability induces a tightened droplet distribution. We explain the two peaks by the fact that in the traditional Plateau Rayleigh break-up we can often observe a main droplet diameter and the emission of secondary droplet much smaller.

**B.  Case of $N$ triangular prisms ($R_p = 15$ mm)**

In the following, we now investigate the effects of $N$ triangular prisms on the droplet diameter distribution. Due to the potential applications of this study, we wanted to maximize the number of jets and therefore we choose $b = 0.25$ mm. To stay in the $n = N$ regime we keep $Q = 2.8\ 10^{-5}$ m$^3$.s$^{-1}$. We study the influence of $a_p$ (keeping values compatible with the $n = N$ regime) on the droplet diameter distribution. A synthesis of the three designs studied here is presented in Table III.

TABLE III: Characteristics of droplets corresponding to three tested designs $TD_1$, $TD_2$ and $TD_3$ measured at $R_p = 15$ mm. The *disk without prisms* corresponds to the reference case. All the measurements were performed for $Q = 2.8\ 10^{-5}$ m$^3$.s$^{-1}$.

| | $b$ (mm) | $a_p$ (mm) | number of prisms $N$ | $D_m$ ($\mu$m) | $STD$ ($\mu$m) | $CV$ (%) |
|---|---|---|---|---|---|---|
| *Disk without prisms* | | | | 331 | 123 | 37 |
| $TD_1$ | 0.25 | 1.06 | 72 | 602 | 233 | 38 |
| $TD_2$ | 0.25 | 0.85 | 86 | 460 | 210 | 45 |
| $TD_3$ | 0.25 | 0.75 | 94 | 424 | 186 | 44 |

Figure 18 presents the droplet percentages as a function of their diameters. The three tested designs $TD_1$, $TD_2$ and $TD_3$ (see Figure 16) are compared to the case of a disk without prisms.

In this configuration, we recover the bimodal structure previously observed. The lower $a_p$ is, the narrower the peaks are and therefore the higher is their amplitude. We observe
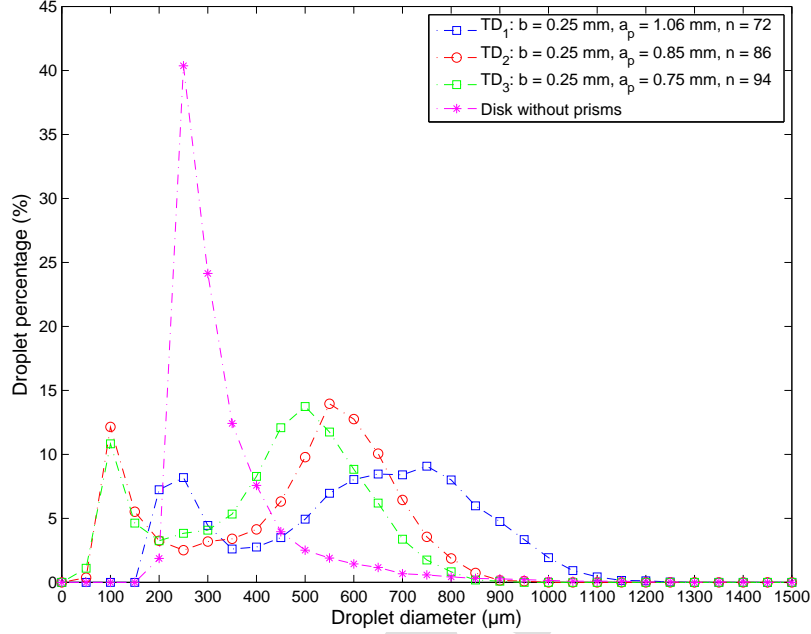
FIG. 18: Representation of droplet percentages as a function of their diameters in the case of three designs $TD_1$, $TD_2$ and $TD_3$. The prisms are placed at $R_p = 15$mm from the jet impact. The curve *disk without prisms* corresponds to droplets emitted from the Savart sheet. All the measurements were performed for $Q = 2.8 \; 10^{-5} \; \text{m}^3.\text{s}^{-1}$.

that the positions of the peaks are also affected by $a_p$: the smaller $a_p$ is, the smaller the emitted drops are. The position of the first peak evolves from ~250 $\mu$m to ~100 $\mu$m as $a_p$ decreases and the second peak from ~750 $\mu$m to ~500 $\mu$m.

We interpret these results as follow: the droplets are still issue from the Plateau Rayleigh instability and it still explains the bimodal behavior. However, the triangular prism are sharpened, therefore we obtained more controlled liquid jets. It results in a tightened distribution and smaller emitted droplets.

### C. Case of $N$ triangular prisms ($R_p =$ variable)

Finally, we address the question of the effects of $N$ triangular prisms on the droplet diameter distribution but with $R_p$ varying from 15 mm to 30 mm. As previously mentioned, the upper limitation for $R_p$ is $R'$, therefore we are still in the continuous and plain part of the liquid sheet. The other characteristics are still unchanged: $b = 0.25$ mm, $a_p = 1.06$ mm and $Q = 2.8 \; 10^{-5} \; \text{m}^3.\text{s}^{-1}$. This guarantees that we are still in the $n = N$ regime. All this information is summarized in Table IV.

Figure 19 shows the droplet percentages as a function of their diameters. The three tested designs $TD_1$, $TD_4$ and $TD_5$ are compared to the case of a disk without prisms.

In this configuration, we recover the bimodal structure previously observed. The position of the prisms, $R_p$, mainly affects the peak positions and the amplitude of the first peak. The position of the first peak evolves from ~250 $\mu$m to ~100 $\mu$m as $R_p$ increases and the second peak from ~750 $\mu$m to ~400 $\mu$m. Since the diameter distribution is tightened the amplitude of the first peak increases from 7% to 15% when $R_p$ increases.

We may interpret these results by the fact that the Savart liquid sheet thickness decreases

TABLE IV: Characteristics of droplets corresponding to three tested designs $TD_1$, $TD_4$ and $TD_5$ measured at three $R_p$ values that are respectively 15 mm, 22 mm and 28 mm. The *disk without prisms* corresponds to the reference case. All the measurements were performed for $Q = 2.8 \ 10^{-5} \ \text{m}^3.\text{s}^{-1}$.

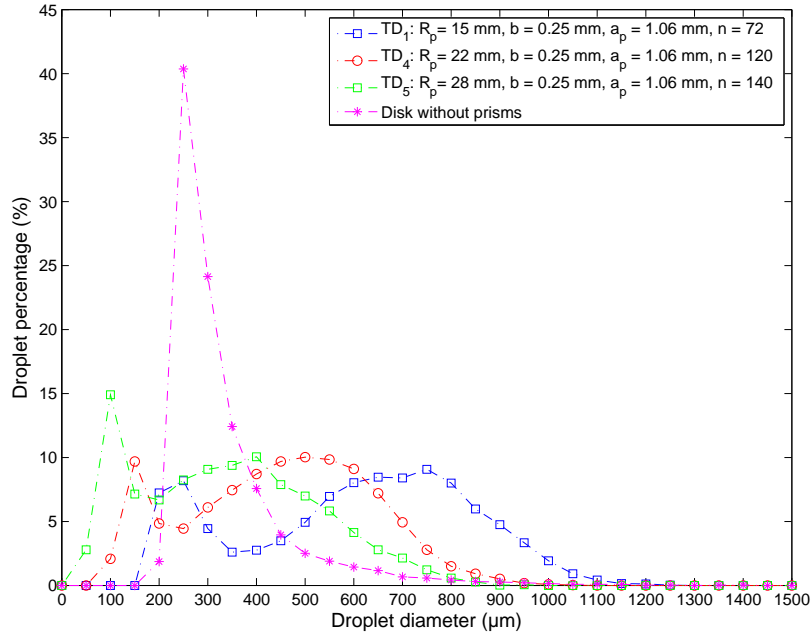| | $R_p$ (mm) | $b$ (mm) | $a_p$ (mm) | number of prisms $N$ | $D_m$ ($\mu$m) | $STD$ ($\mu$m) | $CV$ (%) |
|---|---|---|---|---|---|---|---|
| *Disk without prisms* | | | | | 331 | 123 | 37 |
| $TD_1$ | 15 | 0.25 | 1.06 | 72 | 602 | 233 | 38 |
| $TD_4$ | 22 | 0.25 | 1.06 | 120 | 447 | 187 | 41 |
| $TD_5$ | 28 | 0.25 | 1.06 | 140 | 337 | 183 | 54 |



FIG. 19: Representation of droplet percentages as a function of their diameters in the case of three designs $TD_1$, $TD_4$ and $TD_5$. The prisms are placed at different $R_p$ that are 15 mm, 22 mm and 28 mm. The reference case corresponds to the *disk without prisms*. All the measurements were performed for $Q = 2.8 \ 10^{-5} \ \text{m}^3.\text{s}^{-1}$.

when the radial position increases. Therefore, the liquid sheet is thinner when it interacts with the triangular prisms and hence it leads to smaller droplets.

To conclude this section on the droplet diameter distribution, we can sum up all the studied designs in Figure 20. In all the configurations, we observe a bimodal distribution, which we attribute to Plateau Rayleigh instability. The smaller $b$ is, the higher the second peak amplitude is. This distribution may be shifted to smaller value of droplet diameter by increasing $R_p$ or by decreasing $a_p$. These variations for these two parameters also lead to the increase of $N$ since $N \approx \frac{2\pi R_p}{a_p + b}$. This is of interest for potential applications and especially for the design of agricultural nozzles.
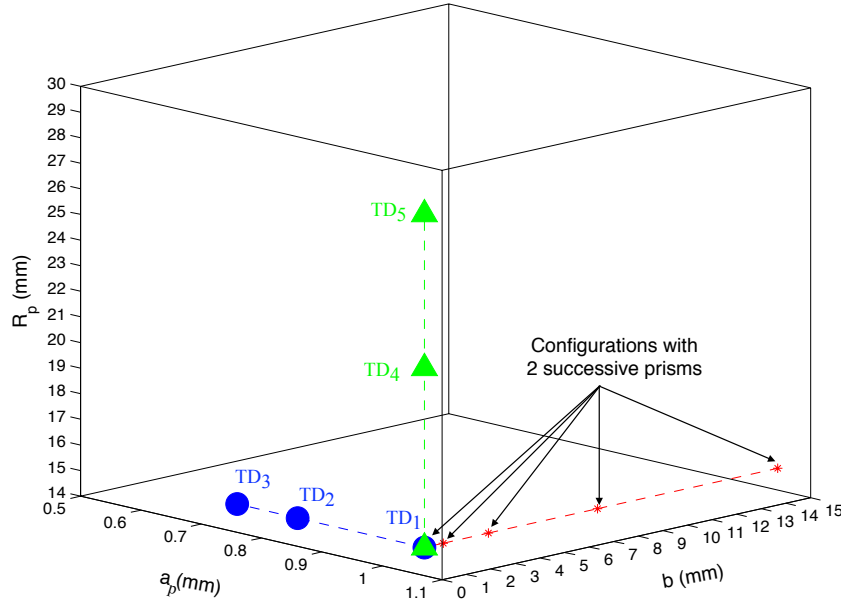
FIG. 20: 3D representation of the parameters $a_p$, $b$ and $R_p$ corresponding to different disk configurations.

## VI. CONCLUSION

In this article, we have reported the splitting of a non-laminar Savart sheet into individual jets by mean of triangular prisms. We characterized the non-laminar Savart sheet, its ejection angle $\phi$, its radial expansion $R$ and the intermediate region $R' < r < R$ where holes due to puncturing appear in the liquid sheet.

Based on this information, we placed triangular prisms at $r < R'$ in order to efficiently fragment the flow into liquid jets. We first studied the physical objects resulting of the opening of the liquid sheet by two triangular prisms separated by the distance $b$: depending on the value of $b$ we observed Savart sheet converging into a jet ($vss$) or liquid ligaments. We suggested a simple geometrical model able to describe roughly the length of the $vss$.

We then studied the case of $N$ triangular prisms regularly placed all along a crown stated at a radial distance $r < R'$. We observed two regimes depending on the flow rate, $b$ and the prism base $a_p$: the $n = N$ regime and the $\frac{N}{2} \leq n < N$ regime. This last regime is unstable due to elastic coalescence phenomena.

Finally, we rationalized the sizes of the droplets emitted from our experiments. We reported a bimodal distribution that can be adjusted using $b$, $a_p$ and $R_p$ the radial position of the triangular prisms.

The mechanism of the sheet rupture is still to be analyzed and this analysis has to include the measurement of the local thickness $h(r)$ of the sheet through the "lateral" Weber number $\frac{\rho u_0^2 h}{\gamma}$.

Despite the complexity of the problem, we reached our goal of splitting a non-laminar Savart sheet into $N$ jets over a large $Q$ range. These findings constitutes an advanced step compared to the previous works in the laminar[7] and in the non-laminar regimes[19] and paves to way to future innovations in the field of spray atomization for agricultural purposes.

Indeed, the present configuration presents much flexibility on its geometrical parameters allowing a large number of jets $n$. We obtained properties very close to the best agricultural

nozzles[20] but without the disadvantages in terms of costs and bulkiness.

## ACKNOWLEDGMENTS

## AUTHOR CONTRIBUTION

All authors contributed to the study conception and design. Material preparation, experiments and data collection were performed by Sofiene Ouled Taleb Salah and Ghada chouk. All authors performed data analysis. The supervision was specifically ensured by Frédéric Lebeau and Stéphane Dorbolo. The first draft of the manuscript was written by Sofiene Ouled Taleb Salah and all authors commented on previous versions of the manuscript. Alexis Duchesne has the highest contribution in editing this manuscript. All authors read and approved the final manuscript.

## DATA AVAILABILITY

The data that support the findings of this study are available from the corresponding author upon reasonable request.

[1] Philippe Brunet, Christophe Clanet, and Laurent Limat. Transonic liquid bells. Physics of Fluids, 16:2668–2678, 2004.

[2] Christophe Clanet. Les nappes d'eau de félix savart. Bulletin National de la SFP, 125:11–15, 2000.

[3] Christophe Clanet. Dynamics and stability of water bells. Journal of Fluid Mechanics, 430:111–147, 2001.

[4] Christophe Clanet and Emmanuel Villermaux. Life of a smooth liquid sheet. Journal of fluid mechanics, 462:307–340, 2002.

[5] Nicolas De Cock, Mathieu Massinon, David Nuyttens, Donald Dekeyser, and Frédéric Lebeau. Measurements of reference iso nozzles by high-speed imaging. Crop Protection, 89:105–115, 2016.

[6] Nicolas De Cock, Mathieu Massinon, Sofiene Ouled Taleb Salah, and Frédéric Lebeau. Investigation on optimal spray properties for ground based agricultural applications using deposition and retention models. Biosystems Engineering, 162:99–111, 2017.

[7] Emilie Dressaire, Laurent Courbin, Adrian Delancy, Marcus Roper, and Howard A Stone. Study of polygonal water bells: inertia-dominated thin-film flows over microtextured surfaces. Journal of Fluid Mechanics, 721:46–57, 2013.

[8] Jens Eggers and Emmanuel Villermaux. Physics of liquid jets. Reports on progress in physics, 71:036601, 2008.

[9] Jose Manuel Gordillo, Henri Lhuissier, and Emmanuel Villermaux. On the cusps bordering liquid sheets. Journal of Fluid Mechanics, 754:R1, 2014.

[10] John M Kolinski, Hillel Aharoni, Jay Fineberg, and Eran Sharon. Growth and nonlinear response of driven water bells. Physical Review Fluids, 2:042401, 2017.

[11] Henri Lhuissier, Philippe Brunet, and Stéphane Dorbolo. Blowing a liquid curtain. Journal of Fluid Mechanics, 795:784–807, 2016.

[12] Nayanika Majumdar and Mahesh S Tirumkudulu. Dynamics of radially expanding liquid sheets. Physical review letters, 120(16):164501, 2018.

[13] Graham Matthews. Pesticide application methods. John Wiley & Sons (2008).

[14] Kimiaki Miyamoto and Yoshinobu Katagiri. Curtain coating. Liquid film coating, Springer, pages 463–494, 1997.

[15] Baptiste Néel and Emmanuel Villermaux. The spontaneous puncture of thick liquid films. Journal of Fluid Mechanics, 838:192–221, 2018.

[16] Manjula Paramati and Mahesh S Tirumkudulu. Open water bells. Physics of Fluids, 28:032105, 2016.

[17] Jean-Yves Parlange. A theory of water-bells. Journal of Fluid Mechanics, 29:361–372, 1967.

[18] Osborne Reynolds. Xxix. an experimental investigation of the circumstances which determine whether the motion of water shall be direct or sinuous, and of the law of resistance in parallel channels. Philosophical Transactions of the Royal society of London, (174):935–982, 1883.

[19] Sofiene Ouled Taleb Salah, Alexis Duchesne, Nicolas De Cock, Mathieu Massinon, Khaled Sassi, Khaoula Abrougui, Frédéric Lebeau, and Stéphane Dorbolo. Experimental investigation of a round jet impacting a disk engraved with radial grooves. European Journal of Mechanics-B/Fluids, 72:302–310, 2018.

[20] Sofiene Ouled Taleb Salah, Mathieu Massinon, Bruno Schiffers, and Frédéric Lebeau. Use of rotary atomiser to optimize retention on barley leaves while reducing driftable droplets. International Advances in Pesticide Application, Aspects of Applied Biology, 122:237–244, 2014.

[21] Félix Savart. Mémoire sur la constitution des veines liquides lancées par des orifices circulaires en mince paroi. Annales de Chimie et de Physique, 53:337–386, 1833.

[22] Félix Savart. Mémoire sur le choc d'une veine liquide lancée contre un plan circulaire. Annales de chimie, 54:56–87, 1833.

[23] Geoffrey Ingram Taylor. The dynamics of thin-sheets of fluid. i. water bells. Proceedings of the Royal Society of London. Series A: Mathematical, Physical and Engineering Sciences, 253:289–295, 1959.

[24] Geoffrey Ingram Taylor. The dynamics of thin sheets of fluid. iii. disintegration of fluid sheets. Proceedings of the Royal Society of London. Series A: Mathematical, Physical and Engineering Sciences, 253:313–321, 1959.

[25] G Thunivumani and Hrishikesh Gadgil. Dynamics of liquid sheet breakup in splash plate atomization. Journal of Fluids Engineering, 140:011205, 2018.

[26] Chetankumar S Vegad, Satyanarayanan R Chakravarthy, and Amit Kumar. Dynamics of a radially expanding circular liquid sheet and its atomization characteristics. Fire Safety Journal, 100:51–63, 2018.

[27] Emmanuel Villermaux. Fragmentation versus cohesion. Journal of Fluid Mechanics, 898:1, 2020.

[28] Emmanuel Villermaux and Christophe Clanet. Life of a flapping liquid sheet. Journal of fluid mechanics, 462:341–363, 2002.

[29] WH Walton and WC Prewett. The production of sprays and mists of uniform drop size by means of spinning disc type sprayers. Proceedings of the Physical Society. Section B, 62:341, 1949.

[30] Y Wang and L Bourouiba. Unsteady sheet fragmentation: droplet sizes and speeds. Journal of Fluid Mechanics, 848:946–967, 2018.

[31] Jun Zhang, Peng-Fei Liang, Ying Luo, Ying Guo, and You-Zhi Liu. Liquid sheet breakup mode and droplet size of free opposed impinging jets by particle image velocimetry. Industrial & Engineering Chemistry Research, 59:11296–11307, 2020.

- A turbulent liquid jet impinging on a plane gives birth to a punctured Savart sheet

- Using triangular prisms, it is possible to divide a liquid Savart sheet into jets.

- To control the shape of the jets we change the distance between prisms.

- The droplet size distribution issued from liquid jets is bimodal.

- The position and the arrangement of prisms influence the droplet size distribution.

All authors contributed to the study conception and design. Material preparation, experiments and data collection were performed by Sofiene Ouled Taleb Salah and Ghada chouk. Data analysis was performed by all authors. The supervision was specifically ensured by Frédéric Lebeau and Stéphane Dorbolo. The first draft of the manuscript was written by Sofiene Ouled Taleb Salah and all authors commented on previous versions of the manuscript. Alexis Duchesne has the highest contribution in editing this manuscript. All authors read and approved the final manuscript.

**Declaration of interests**

☒ The authors declare that they have no known competing financial interests or personal relationships that could have appeared to influence the work reported in this paper.

☐The authors declare the following financial interests/personal relationships which may be considered as potential competing interests:

<br/>